






Evolution of Magnetic Helicity in Solar Cycle 24

Valery V. Pipin¹ , Alexei A. Pevtsov^{2,3} , Yang Liu⁴, and Alexander G. Kosovichev⁵ 

¹Institute for Solar-Terrestrial Physics, P.O. Box 291, Lermontov st., 126a, Irkutsk, 664033, Russia; pip@iszf.irk.ru

²National Solar Observatory, 3665 Discovery Drive, 3rd Floor, Boulder, CO 80303, USA

³Central Astronomical Observatory of RAS at Pulkovo, Saint Petersburg, 196140, Russia

⁴Stanford University, Stanford, CA, USA

⁵New Jersey Institute of Technology, Newark, NJ, USA

Received 2019 April 22; revised 2019 May 10; accepted 2019 May 15; published 2019 June 4

Abstract

We propose a novel approach to reconstruct the surface magnetic helicity density on the Sun or Sun-like stars. The magnetic vector potential is determined via decomposition of vector magnetic-field measurements into toroidal and poloidal components. The method is verified using data from a non-axisymmetric dynamo model. We apply the method to vector field synoptic maps from the Helioseismic and Magnetic Imager on board the *Solar Dynamics Observatory* to study the evolution of the magnetic helicity density during solar cycle 24. It is found that the mean helicity density of the non-axisymmetric magnetic field of the Sun evolves in a way similar to that reported for the current helicity density of the solar active regions. It predominantly has a negative sign in the northern hemisphere, while it is mainly positive in the southern hemisphere. Also, the hemispheric helicity rule for the non-axisymmetric magnetic field showed the sign inversion at the end of cycle 24. The evolution of the magnetic helicity density of a large-scale axisymmetric magnetic field is different from what is predicted by dynamo theory. On one hand, the mean large- and small-scale components of magnetic helicity density display the hemispheric helicity rule of opposite signs at the beginning of cycle 24. However, later in the cycle, the two helicities exhibit the same sign, in contrast with theoretical expectations.

Key words: Sun: activity – Sun: fundamental parameters – Sun: magnetic fields

1. Introduction

Magnetic helicity is an integral measure of topological properties of the magnetic field in closed volume V :

$$H_M = \int \mathbf{A} \cdot \mathbf{B} dV, \quad (1)$$

where \mathbf{A} is the magnetic vector potential, $\mathbf{B} = \nabla \times \mathbf{A}$, and \mathbf{B} is confined to the volume V . Locally, it can be characterized by a number of parameters such as linkage, twist, and writhe of the field lines (Berger & Hornig 2018). In astrophysical dynamos, magnetic helicity is commonly regarded as a nonlinear constraint of the turbulent generation of a large-scale magnetic field (Pouquet et al. 1975; Kleeorin & Ruzmaikin 1982; Brandenburg & Subramanian 2005). Computation of the magnetic helicity on the Sun requires knowledge of the vector magnetic field in a 3D region, but observations are usually taken in a shallow layer of the solar atmosphere (typically, in the photosphere). Thus, early studies turned to calculation of so-called helicity proxies, such as, for example, vertical components of current helicity density $J_z \cdot B_z$ or $\alpha = J_z/B_z$ (a measure of magnetic twist). Seehafer (1990) and Pevtsov et al. (1995) found that the current helicity density and twist in solar active regions follow *the hemispheric helicity rule*: predominantly negative values in the northern hemisphere and mainly positive values in the southern hemisphere. The hemispheric preference for the helicity sign was later confirmed by several researchers (e.g., Bao & Zhang 1998; Longcope et al. 1998; Hagino & Sakurai 2005). Choudhuri et al. (2004) proposed that due to the interaction of the large-scale toroidal field from a previous solar cycle with the poloidal field of a new cycle, the hemispheric helicity could reverse signs at the beginning of

each cycle. Hagino & Sakurai (2005) reported such a sign reversal in Okayama Observatory Solar Telescope and Mitaka Solar Flare Telescope observations. Pevtsov et al. (2008) examined the periods of sign reversals observed by different instruments and found no agreement among the data sets during these periods. They concluded that at least some reversals could be due to the statistical nature of the hemispheric helicity rule. Later, Zhang et al. (2010) showed that the hemispheric helicity rule of the solar active regions evolves with time and found reversals at the beginning of Solar Cycles 22 and 23. Sokoloff et al. (2013) found inversions of the current helicity density in active regions at the beginning and end of solar cycle 23. These early findings are based on vector magnetograms of active regions only. Systematic full-disk observations of vector magnetic field became available in 2009 from the Vector Spectromagnetograph on the Synoptic Optical Long-term Investigations of the Sun (SOLIS) platform (Balasubramanian & Pevtsov 2011) and in 2010 from the Helioseismic and Magnetic Imager (HMI, Scherrer et al. 2012) on board *Solar Dynamics Observatory* (SDO, Pesnell et al. 2012). Prior to these observations, calculations of current helicity relied on the vector magnetic field reconstructed from rotational modulation of the observed longitudinal (line of sight) field (Pevtsov & Latushko 2000). Later studies demonstrated that the sign of the helicity of large-scale magnetic fields is the opposite of the sign of helicity of active regions (Pipin & Pevtsov 2014; Brandenburg et al. 2017). The large-scale helicity was also found to evolve during solar cycles, similar to the helicity of active regions.

Solar dynamo theory predicts bihelical properties of magnetic fields (Blackman & Brandenburg 2002; Brandenburg

& Subramanian 2005). In this theory the sign of the magnetic helicity density of a large-scale field should correspond to the sign of the α -effect, while the sign of the magnetic helicity density of a small-scale field should result from magnetic helicity conservation, and thus should be the opposite of the large-scale helicity. In the framework of this model, a small-scale magnetic field corresponds to active regions and the large-scale magnetic field represents the global axisymmetric components of the solar magnetic activity. The bihelical properties were studied by Brandenburg et al. (2017) and Singh et al. (2018) using two-scale approximation and the vector magnetic-field measurements from *SDO*/HMI and SOLIS. The results from the two different instruments appear to be inconclusive with respect to the bihelical nature of a solar magnetic field.

Other predictions of mean-field dynamo models include the existence of polar and equatorial branches in the time–latitude diagram of magnetic helicity evolution. According to Pipin et al. (2013), those branches represent the transport of magnetic helicity flux to the polar regions, both on large and small scales. In this paper we present the first observational evidence of polar branches of the large-scale magnetic helicity in solar cycle 24. Section 2 describes how we calculated the magnetic helicity. Section 3 verifies the proposed methodology using synthetic data from mean-field dynamo model calculations. Section 4 presents the derivation of magnetic helicity using observed magnetic fields, and Section 5 discusses our findings.

2. The Method

To determine the magnetic helicity density, we employ a decomposition of the vector magnetic field into toroidal and poloidal components using scalar potentials S and T (Krause & Rädler 1980; Berger & Hornig 2018):

$$\begin{aligned} \mathbf{B} &= \nabla \times (\hat{\mathbf{r}}T) + \nabla \times \nabla \times (\hat{\mathbf{r}}S) \\ &= -\frac{\hat{\mathbf{r}}}{r} \Delta_{\Omega} S + \hat{\theta} \left(\frac{1}{\sin \theta} \frac{\partial T}{\partial \phi} - \frac{\sin \theta}{r} \frac{\partial F_S}{\partial \mu} \right) \\ &\quad + \hat{\phi} \left(\sin \theta \frac{\partial T}{\partial \mu} + \frac{1}{r \sin \theta} \frac{\partial F_S}{\partial \phi} \right) \end{aligned} \quad (2)$$

where $\Delta_{\Omega} = \frac{\partial}{\partial \mu} \sin^2 \theta \frac{\partial}{\partial \mu} + \frac{1}{\sin^2 \theta} \frac{\partial^2}{\partial \phi^2}$, $\mu = \cos \theta$, and θ is the polar angle, and $F_S = \partial(rS)/\partial r$. Three components of vector magnetic field (radial r , meridional θ , and zonal ϕ , see, Virtanen et al. 2019) are then represented by three independent variables, S , T , and F_S :

$$B_r = -\frac{1}{r} \Delta_{\Omega} S, \quad (3)$$

$$B_{\theta} = \frac{1}{\sin \theta} \frac{\partial T}{\partial \phi} - \frac{\sin \theta}{r} \frac{\partial F_S}{\partial \mu}, \quad (4)$$

$$B_{\phi} = \sin \theta \frac{\partial T}{\partial \mu} + \frac{1}{r \sin \theta} \frac{\partial F_S}{\partial \phi}. \quad (5)$$

To determine a unique solution for Equations (3)–(5) we apply the following gauge (see, e.g., Krause & Rädler 1980):

$$\int_0^{2\pi} \int_{-1}^1 S d\mu d\phi = \int_0^{2\pi} \int_{-1}^1 T d\mu d\phi = \int_0^{2\pi} \int_{-1}^1 F_S d\mu d\phi = 0. \quad (6)$$

Note, that in the case of potential magnetic field $T = 0$, and F_S is determined by S . Therefore, the system of Equations (3)–(5) represents a least-squares problem. Hereafter we consider the general case of nonpotential magnetic fields on the solar surface. Equations (3)–(5) can be transformed into

$$-\frac{1}{r} \Delta_{\Omega} S = B_r, \quad (7)$$

$$\Delta_{\Omega} T = \frac{\partial}{\partial \mu} \sin \theta B_{\phi} + \frac{1}{\sin \theta} \frac{\partial B_{\theta}}{\partial \phi}, \quad (8)$$

$$\frac{1}{r} \Delta_{\Omega} F_S = \frac{1}{\sin \theta} \frac{\partial B_{\phi}}{\partial \phi} - \frac{\partial}{\partial \mu} \sin \theta B_{\theta}. \quad (9)$$

Reconstruction and differentiating is done in the spectral spherical harmonic space using the SHTools (Wieczorek & Meschede 2018). After finding solutions for S , T , and F_S we can determine components of vector potential \mathbf{A} ,

$$\begin{aligned} \mathbf{A} &= \hat{\mathbf{r}}T + \nabla \times (\hat{\mathbf{r}}S) \\ &= \hat{\mathbf{r}}T + \frac{\hat{\theta}}{\sin \theta} \frac{\partial S}{\partial \phi} + \hat{\phi} \frac{\sin \theta}{r} \frac{\partial S}{\partial \mu}. \end{aligned} \quad (10)$$

Below we demonstrate the method using the output of a dynamo model, where we have complete information about the distribution of the vector magnetic field, its vector potential, and the magnetic helicity density.

Following the standard framework of mean-field magneto-hydrodynamics, we decompose the magnetic field and its vector potential into the mean and fluctuating parts $\mathbf{B} = \overline{\mathbf{B}} + \mathbf{b}$, $\mathbf{A} = \overline{\mathbf{A}} + \mathbf{a}$, where the small letters represent small-scale fluctuations and the capital letters with over-bars represent large-scale fields. Theoretically, the large-scale magnetic field (or the mean field) is defined as an average over an ensemble of fluctuating magnetic-field states (Krause & Rädler 1980). In practice, to determine the large- and small-scale magnetic-field components we apply a two-scale approximation, and assume that the spatial and temporal scales of the mean magnetic field are much larger than those of the small-scale fields. In the case of solar magnetism, the timescale of the mean magnetic field corresponds to the solar cycle period and the small-scale magnetic field varies on much shorter intervals corresponding to the typical timescale of evolution of solar active regions. The solar dynamo predominantly operates in an axisymmetric dynamo regime (Krause & Rädler 1980; Rädler 1986; Pipin & Kosovichev 2018). Therefore, we can express the relationship between the magnetic helicity density of the large- and small-scale magnetic fields as follows:

$$\overline{\mathbf{a} \cdot \mathbf{b}} = \overline{\mathbf{A} \cdot \mathbf{B}} - \overline{\mathbf{A}} \cdot \overline{\mathbf{B}}. \quad (11)$$

Thus, the small-scale magnetic helicity density $\overline{\mathbf{a} \cdot \mathbf{b}}$ includes magnetic fields from all ranges of scales, except the axisymmetric magnetic field.

3. Dynamo Model Benchmark

We use results of the non-axisymmetric $\alpha^2\Omega$ dynamo model developed recently by Pipin & Kosovichev (2018). The model simulates the solar-type dynamo in which the surface magnetic activity is governed by the dynamo-generated axisymmetric toroidal magnetic field. The dynamo parameters of the model are below the threshold of the dynamo instability of large-scale non-axisymmetric magnetic fields. This resembles the situation

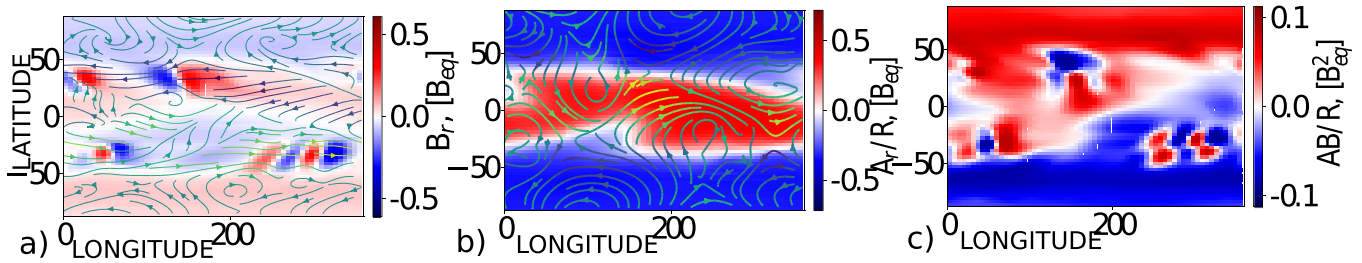


Figure 1. (a) Snapshot of the radial magnetic-field distribution (color image); the streamlines show the horizontal (toroidal and poloidal) magnetic field. (b) Snapshot of the magnetic helicity density. (c) The radial component of the current helicity density $H_C = B_r(\nabla \times \mathbf{B})_r$.

for solar-type dynamos (Raedler 1986). In order to mimic the emergence of solar active regions, we take into account the Parker’s magnetic buoyancy instability, which produces bipolar regions from the toroidal magnetic field at random latitudes and random moments of time under the condition that the magnetic-field strength exceeds a critical threshold. The reader can find a detailed description of the model and the code in Pipin & Kosovichev (2018) and Pipin (2018).

Figure 1 shows snapshots of the magnetic-field components, as well as the magnetic and current helicity densities. The snapshots are taken during the maximum of the dynamo cycle. The magnetic helicity has a predominantly positive sign in the northern hemisphere and a predominantly negative sign in the southern hemisphere. In this case, the hemispheric helicity rule of the large-scale magnetic field follows from dynamo theory, which predicts that the sign of the magnetic helicity of the large-scale field corresponds to the sign of the α -effect in a given hemisphere (Blackman & Brandenburg 2003; Singh et al. 2018).

4. Magnetic Helicity Density Derived from Observations

4.1. Observational Data

We apply the formalism described in Section 2 to a set of intermediate-resolution (360 by 720 pixels) vector magnetic fields synoptic maps from HMI/*SDO*. The data set includes 116 Carrington rotations (CR) from CR 2097 (2010 May) to CR 2214 (2019 March). The HMI synoptic maps are calculated in a Carrington longitude (degrees)–sine (latitude) coordinate grid. The pixel size is 0.5° in longitude and $1/180$ in sine latitude. The method for producing the HMI synoptic maps is described in detail in Liu et al. (2017). For these data, the 180° ambiguity in the horizontal field direction was resolved by the HMI team using a combination of a minimum energy criterion (for pixels with stronger fields) and random disambiguation (for weak field pixels). Additional details about the HMI data reduction and the disambiguation procedure can be found in the above cited paper.

Liu et al. (2017) found that with the chosen combination of disambiguation methods the noise level of the vector magnetic field in the synoptic charts varies from ± 10 G during the solar maximum to ± 20 G during the solar minimum.

4.2. Results

As the first example, we consider the results of reconstruction of the vector potential for the synoptic maps of CR 2156. This CR is characterized by the strong active region NOAA AR 12192, which emerged in the southern hemisphere. Figure 2 shows the synoptic maps of the vector magnetic field and the reconstructed potentials S , $A_r = rT$. The distribution of

the vector potential reveals a large-scale non-axisymmetric pattern associated with this active region. Note that the vector-potential components show an inverse sign relative to the corresponding magnetic-field components in the core of the active region. This results in a predominantly negative magnetic helicity in AR 12192, which is shown in Figure 3. We notice that the east part of the southern hemisphere shows the background magnetic helicity of the positive sign, which corresponds to the basic hemispheric helicity of the active regions (Pevtsov et al. 2014). The large area of the negative magnetic helicity density around NOAA AR 12192 resembles the situation demonstrated in our dynamo model. Thus, it can be speculated that the origin of this active region is related to the large-scale magnetic field located in a shallow subsurface layer.

Solving Equations (3)–(5) for each CR from CR 2097 to CR 2214, we derived the distributions of the vector potential and magnetic helicity density for solar cycle 24. The large-scale distributions of magnetic field and helicity density are obtained by means of the azimuthal averaging of the synoptic maps for each CR. To represent the mean signal, we filtered out the time variations with periods less than 2 yr. Also, we employ the Gaussian smoothing with an FWHM equal to 5 pixels in latitude and 10 CR time. Figure 4 shows the time–latitude diagrams for the axisymmetric components of the magnetic field and vector potential. The time–latitude diagrams of the magnetic-field evolution are in agreement with Vidotto et al. (2018). The reconstructed potentials disagree with the results of Pipin & Pevtsov (2014), who used profiles of \bar{B}_r from different longitudinal distances from the central meridian to reconstruct \bar{B}_ϕ and \bar{A}_r . Also, the obtained \bar{B}_ϕ disagrees with our results at the polarward side of the sunspot activity zone, where the large-scale toroidal magnetic field is present. The sign of this field is the opposite of that of the toroidal field in the solar active regions. Such a bimodal structure of the axisymmetric toroidal magnetic field affects the distribution of \bar{A}_r . The sign of the polarward side of the axisymmetric toroidal magnetic field can hardly be explained by the surface effect of the differential rotation acting on the meridional component of the axisymmetric magnetic field. Also, in our case, the evolution of \bar{A}_ϕ differs from the results of Stenflo & Guedel (1988), Blackman & Brandenburg (2003), and Pipin & Pevtsov (2014) as well, who found symmetric \bar{A}_ϕ profiles relative to the equator. The difference is likely due to the rather asymmetric development of Cycle 24 in the northern and southern hemispheres.

Figure 5(a) shows the time–latitude diagrams of the magnetic helicity density of the large-scale field, $\bar{\mathbf{A}} \cdot \bar{\mathbf{B}}$. The magnetic helicity of the large-scale field is positive in the high-latitude zone of the northern hemisphere at the beginning of

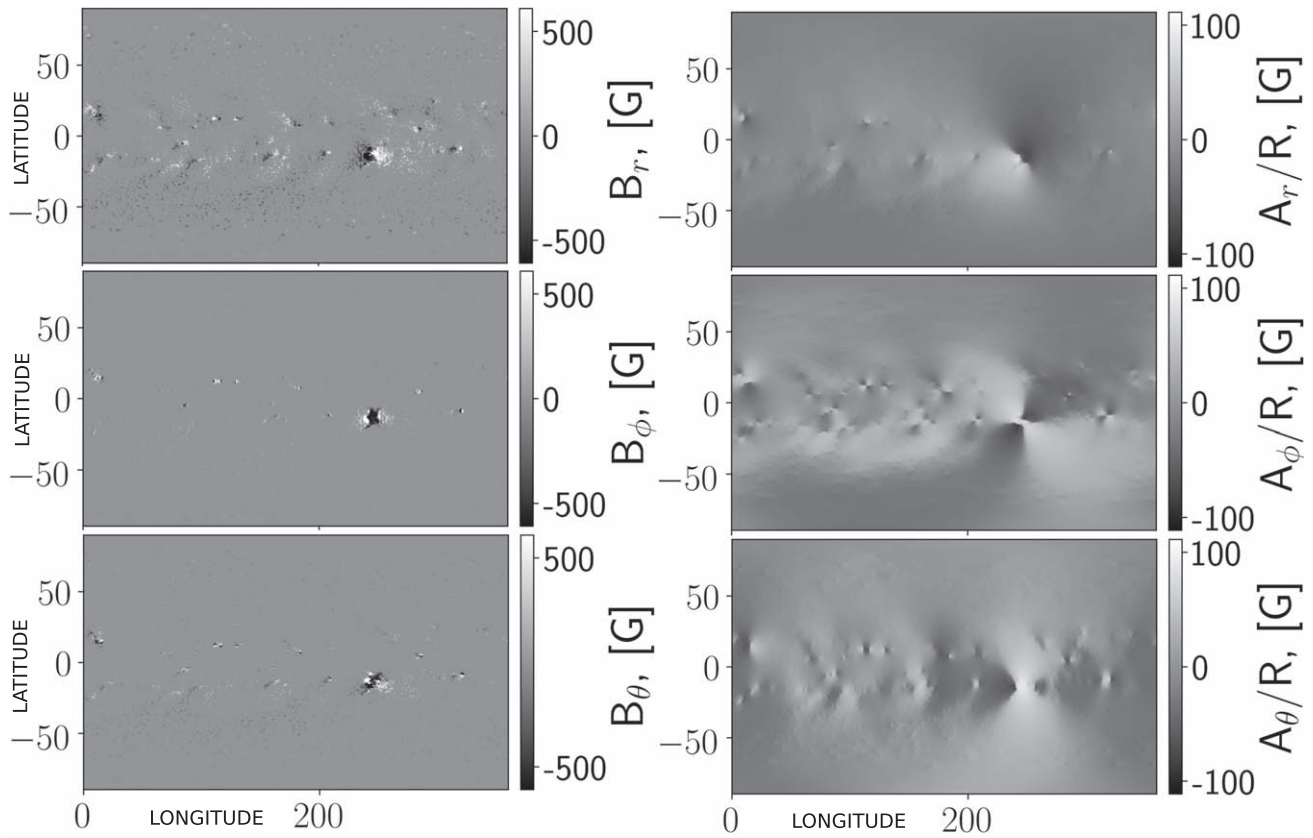


Figure 2. Synoptic maps of the vector magnetic field and the reconstructed potential from *SDO/HMI* for CR 2156.

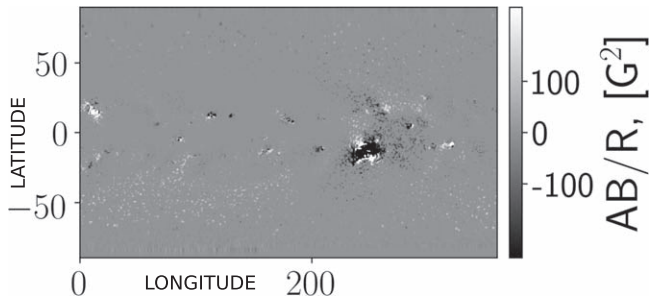


Figure 3. Distribution of the magnetic helicity density $\mathbf{A} \cdot \mathbf{B}$ for CR 2156.

Cycle 24, and it becomes negative after the polar field reversal. A similar situation is observed in the southern hemisphere. Figure 5(b) shows the time-averaged hemispheric helicity sign rule together with uncertainty bars. The uncertainties are estimated using the differences between the original and smoothed signals. It is seen that on average during cycle 24, the large-scale magnetic field shows the same hemispheric sign as the “small-scale” magnetic field. However, if we were to restrict the averaging period to the first half of cycle 24, i.e., by CR 2097–2156, we get, in general, a positive magnetic helicity density in the northern hemisphere and a negative one in the southern hemisphere (except at low latitudes). Therefore, at this period in time the bihelical property can be confirmed with some reservations. This agrees with the two-scale analysis of Brandenburg et al. (2017), as well as with the results of Pipin & Pevtsov (2014; see Figure 9(a) there). Also, Figures 5(c) and (d) support this conclusion.

Figure 5(c) shows the evolution of “small-scale” magnetic helicity density $\mathbf{a} \cdot \mathbf{b}$; see Equation (11). In our definition $\mathbf{a} \cdot \mathbf{b}$

includes magnetic fields from all ranges of scales, except the axisymmetric magnetic field. A more accurate analysis of the magnetic helicity distribution over the scales can be done using the two-scale analysis introduced by Brandenburg et al. (2017). Averaged over cycle $\overline{\mathbf{a} \cdot \mathbf{b}}$, their analysis shows the hemispheric helicity rule for the solar active regions. The large uncertainty bars are mostly caused by fluctuations in magnetic flux emergence. It also can be seen that for the first half of cycle 24, $\overline{\mathbf{a} \cdot \mathbf{b}}$ maintains the hemispheric helicity rule. The violation of the rule in the time-averaged signal is likely caused by the magnetic activity in the southern hemisphere during 2014–2015. In particular, the active region NOAA 12192 strongly violates the hemispheric helicity rule, as we see in Figure 3. At the end of our observational period, $\overline{\mathbf{a} \cdot \mathbf{b}}$ shows inversion of the helicity sign at low latitudes. This agrees with the results for the current helicity density evolution in cycle 23 (e.g., Zhang et al. 2010).

We find that the standard error for $\overline{\mathbf{A}} \cdot \overline{\mathbf{B}}/R$ is less than 1 G^2 and has reaches maximum at sunspot formation latitudes. Similarly, the standard error of $\overline{\mathbf{a} \cdot \mathbf{b}}/R$ is less than 100 G^2 . Liu et al. (2017) estimated the maximum uncertainty of the vector magnetic-field measurement as $\sim 10\text{--}20 \text{ G}$. Thus, we can conclude that the standard deviation of uncertainty of the determined normalized magnetic vector-potential components is less than 10 G . A more accurate estimate of errors for the magnetic helicity density on each synoptic map requires additional analysis, and will be done in a separate paper.

5. Discussion and Conclusions

Here, we propose a novel approach to reconstruct the surface magnetic helicity density on the Sun and Sun-like stars. The

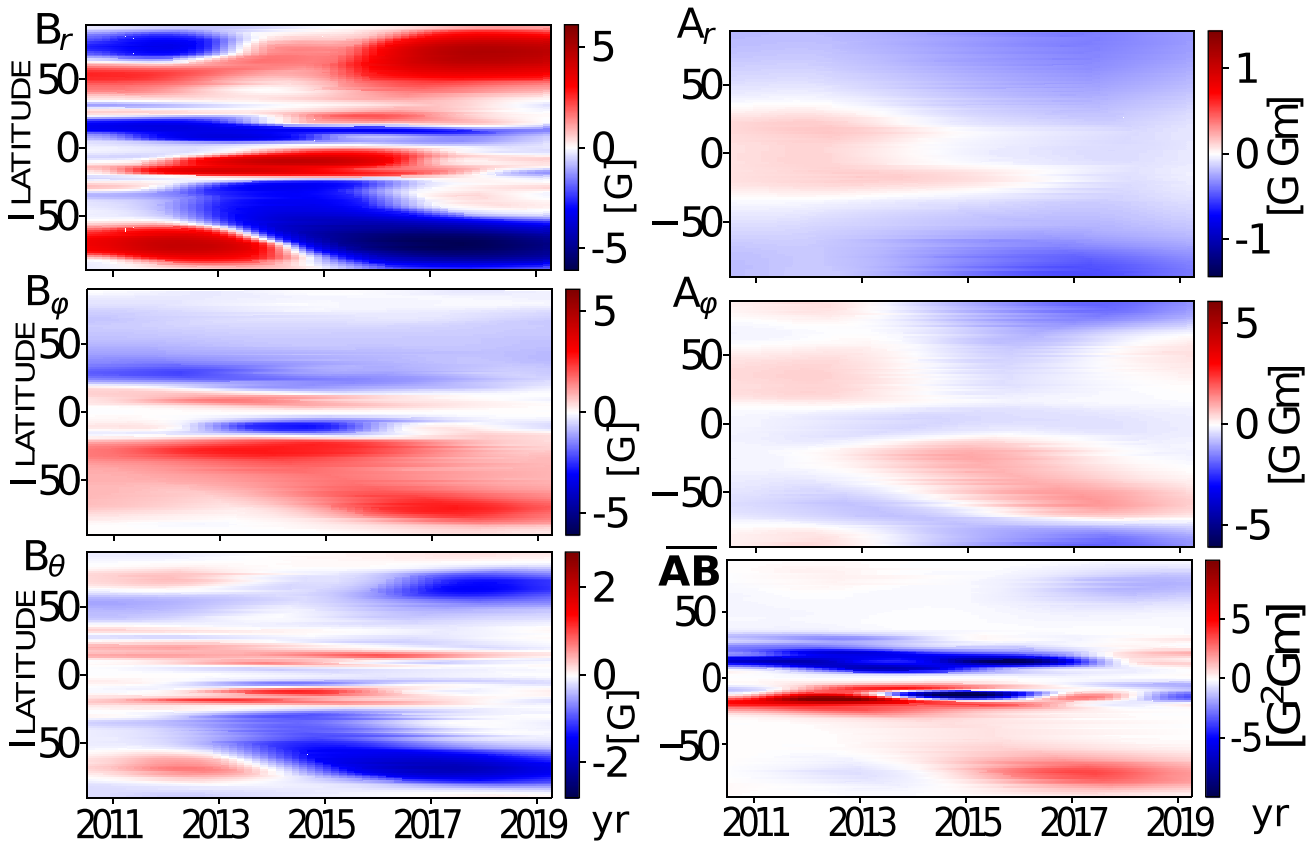


Figure 4. Time–latitude evolution of the large-scale magnetic field : \bar{B}_r , \bar{B}_ϕ , and \bar{B}_θ , as well as the large-scale vector-potential components \bar{A}_r and \bar{A}_ϕ , and the total magnetic helicity density $\bar{A} \cdot \bar{B}$.

magnetic vector potential is determined via decomposition of a vector magnetic field in the toroidal and poloidal components. This method is applied to study the evolution of the magnetic helicity density of large- and small-scale fields in solar cycle 24.

Our results show that at the beginning of cycle 24, the large- and small-scale magnetic helicities are opposite in sign to each other, and both show the hemispheric asymmetry in sign. This is in agreement with magnetic helicity conservation theory (Frisch et al. 1975), which predicts the sign of variations of the small-scale magnetic helicity density, $\mathbf{a} \cdot \mathbf{b}$, should be the opposite of the sign of the large-scale helicity. However, in the declining phase of cycle 24 the large-scale polar magnetic field shows the negative (positive) magnetic helicity in the north (south), which has the same sign as the helicity of the solar active regions (small-scale field). Apparently, in the polar regions the large-scale helicity, $\bar{A} \cdot \bar{B}$, changed sign near the solar maximum. The dynamo models predict that both $\bar{A} \cdot \bar{B}$ and $\mathbf{a} \cdot \mathbf{b}$ can change sign over the course of the solar cycle due to other sources of magnetic helicity evolution, like the turbulent eddy diffusivity of the large-scale magnetic field (Kleeorin & Ruzmaikin 1982; Pipin et al. 2013; Sokoloff et al. 2013). Another possible reason is the magnetic helicity flux escape from the solar surface (Berger & Ruzmaikin 2000). We also note that the dynamo models of (Pipin et al. 2013) predict another polar inversion of the large-scale magnetic helicity models during solar minima. Thus, we expect that the magnetic helicity of a large-scale (polar field) will reverse its sign again around the solar minimum, which would restore the

hemispheric helicity rule to the to its initial conditions at the beginning of cycle 24.

The amplitude of the magnetic helicity of large-scale fields is significantly (an order of magnitude) smaller than the helicity of small-scale (active region) fields. Thus, active regions appear to be the major contributors to the magnetic helicity observed on the visible solar surface (photosphere). This is further supported by the fact that the emergence of a single (large) active region could affect the hemispheric sign preference of helicity for some CR.

In our data we see that the magnetic helicity densities of the large- and small-scale fields often show the same sign in each hemisphere. In our opinion, this might be due to a bimodal distribution of the large-scale toroidal magnetic field on the solar surface. Indeed, we see the two components of the toroidal magnetic field: one is near the equator and another is in the middle latitudes. The near equatorial toroidal field originates from sunspots. The origin of the mid-latitude toroidal field is unclear. This component of the large-scale field can be monohelical over the scales of the magnetic-field distributions in each hemisphere. The evolution of the large-scale magnetic field and its vector potential results in a complicated magnetic helicity evolution. In the data, it is seen that the southern hemisphere was close to the bihelical state during the growing phase of the solar cycle, from 2010 to 2012. The northern hemisphere, except in the polar region, shows the same magnetic helicity density signs for the large- and small-scale fields during that period. Another source of violation of the hemispheric helicity rule is the asymmetric equator development of solar cycle 24. This results in the equatorial

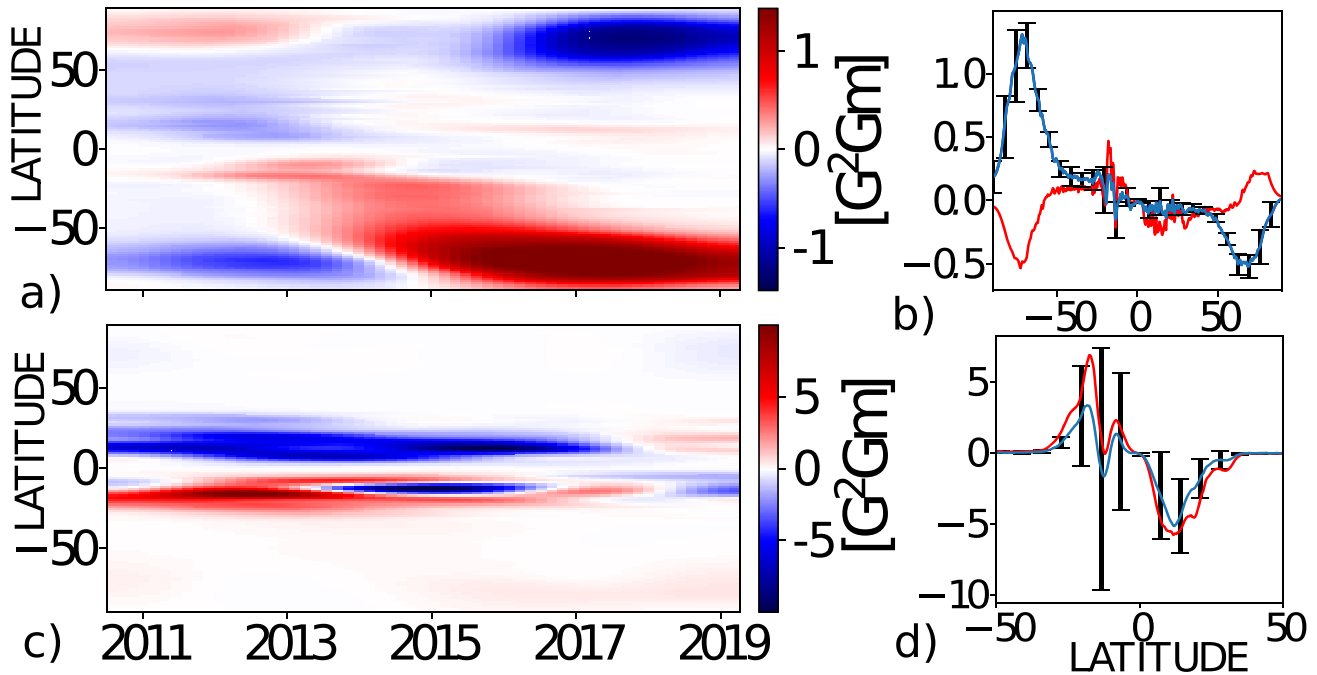


Figure 5. Magnetic helicity in solar cycle 24. (a) The time–latitude evolution of the large-scale magnetic helicity density, $\bar{A} \cdot \bar{B}$. (b) The mean latitudinal profile of the large-scale magnetic helicity density, with a 95% confidence interval for the standard error; the red line shows the average profile for the first half of the cycle including CR 2097–2156. (c) Same as (a) but for the azimuthal averaging of the small-scale magnetic helicity density $\overline{a \cdot b}$; see Equation (11). (d) Same as (b) but for $\overline{a \cdot b}$.

parity breaking in the large-scale magnetic field and vector-potential components. In particular, the obtained evolution of \bar{A}_ϕ is different from previous results by Blackman & Brandenburg (2002) and Pipin & Pevtsov (2014).

The hemispheric helicity rule and bihelical distributions of the solar magnetic fields are essential properties of the solar dynamo operating in the convection zone. We find that in solar cycle 24 these properties of the solar dynamo display a complicated evolution pattern that is not predicted by any current dynamo model.

The surface magnetic helicity does not necessarily match the magnetic helicity in the solar corona. By combining our method with already developed methods of reconstruction of magnetic helicity in the corona, it will be possible to study magnetic helicity transport from the photosphere to the heliosphere, and study variations of the magnetic helicity hemispheric rule with height (Brandenburg et al. 2011).

The suggested method of magnetic helicity reconstruction can be applied to other stars with low-degree modes of the vector magnetic-field distributions, such as those determined in Vidotto et al. (2018). This method can be used to calculate the magnetic vector potential and magnetic helicity density of the large-scale stellar magnetic field.

This work stems from discussions held among the authors during the ‘‘Solar Helicities in Theory and Observations: Implications for Space Weather and Dynamo Theory’’ Program at the Nordic Institute for Theoretical Physics (NORDITA) in 2019 March 4–29. JSOC/HMI maps are courtesy of the NASA/SDO HMI science team. A.A.P. acknowledges partial support by NASA 80NSSC17K0686 and NSF AGS-1620773 grants. A.G.K. was partially supported by NASA grants NNX14AB70G and NNX17AE76A. V.V.P. conducted this work as a part of FR II.16 of ISTP SB RAS; the support of the RFBR grant 19-52-53045 GFEN-a is also acknowledged.

Facility: SDO/HMI.

ORCID iDs

Valery V. Pipin <https://orcid.org/0000-0001-9884-1147>
 Alexei A. Pevtsov <https://orcid.org/0000-0003-0489-0920>
 Alexander G. Kosovichev <https://orcid.org/0000-0003-0364-4883>

References

- Balasubramaniam, K. S., & Pevtsov, A. 2011, *Proc. SPIE*, 8148, 814809
 Bao, S., & Zhang, H. 1998, *ApJL*, 496, L43
 Berger, M. A., & Hornig, G. 2018, *JPhA*, 51, 495501
 Berger, M. A., & Ruzmaikin, A. 2000, *JGR*, 105, 10481
 Blackman, E. G., & Brandenburg, A. 2002, *ApJ*, 579, 379
 Blackman, E. G., & Brandenburg, A. 2003, *ApJL*, 584, L99
 Brandenburg, A., Petrie, G. J. D., & Singh, N. K. 2017, *ApJ*, 836, 21
 Brandenburg, A., & Subramanian, K. 2005, *PhR*, 417, 1
 Brandenburg, A., Subramanian, K., Balogh, A., & Goldstein, M. L. 2011, *ApJ*, 734, 9
 Choudhuri, A. R., Chatterjee, P., & Nandy, D. 2004, *ApJL*, 615, L57
 Frisch, U., Pouquet, A., L  orat, J., & Mazure, A. 1975, *JFM*, 68, 769
 Hagino, M., & Sakurai, T. 2005, *PASJ*, 57, 481
 Kleorin, N. I., & Ruzmaikin, A. A. 1982, *MHD*, 18, 116
 Krause, F., & R  dler, K.-H. 1980, *Mean-Field Magnetohydrodynamics and Dynamo Theory* (Berlin: Akademie-Verlag), 271
 Liu, Y., Hoeksema, J. T., Sun, X., & Hayashi, K. 2017, *SoPh*, 292, 29
 Longcope, D. W., Fisher, G. H., & Pevtsov, A. A. 1998, *ApJ*, 507, 417
 Pesnell, W. D., Thompson, B. J., & Chamberlin, P. C. 2012, *SoPh*, 275, 3
 Pevtsov, A. A., Berger, M. A., Nindos, A., Norton, A. A., & van Driel-Gesztelyi, L. 2014, *SSRv*, 186, 285
 Pevtsov, A. A., Canfield, R. C., & Metcalf, T. R. 1995, *ApJL*, 440, L109
 Pevtsov, A. A., Canfield, R. C., Sakurai, T., & Hagino, M. 2008, *ApJ*, 677, 719
 Pevtsov, A. A., & Latushko, S. M. 2000, *ApJ*, 528, 999
 Pipin, V. 2018, *VVPipin/2DSPDy 0.1.1*, Zenodo, doi:10.5281/zenodo.1413149
 Pipin, V. V., & Kosovichev, A. G. 2018, *ApJ*, 867, 145
 Pipin, V. V., & Pevtsov, A. A. 2014, *ApJ*, 789, 21
 Pipin, V. V., Zhang, H., Sokoloff, D. D., Kuzanyan, K. M., & Gao, Y. 2013, *MNRAS*, 435, 2581

- Pouquet, A., Frisch, U., & Léorat, J. 1975, *JFM*, **68**, 769
- Raedler, K.-H. 1986, *AN*, **307**, 89
- Scherrer, P. H., Schou, J., Bush, R. I., et al. 2012, *SoPh*, **275**, 207
- Seehafer, N. 1990, *SoPh*, **125**, 219
- Singh, N. K., Käpylä, M. J., Brandenburg, A., et al. 2018, *ApJ*, **863**, 182
- Sokoloff, D., Zhang, H., Moss, D., et al. 2013, in *IAU Symp. 294, Solar and Astrophysical Dynamos and Magnetic Activity*, ed. A. G. Kosovichev, E. de Gouveia Dal Pino, & Y. Yan (Cambridge: Cambridge Univ. Press), 313
- Stenflo, J. O., & Guedel, M. 1988, *A&A*, **191**, 137
- Vidotto, A. A., Lehmann, L. T., Jardine, M., & Pevtsov, A. A. 2018, *MNRAS*, **480**, 477
- Virtanen, I. I., Pevtsov, A. A., & Mursula, K. 2019, *A&A*, **624**, A73
- Wieczorek, M., & Meschede, M. 2018, *GGG*, **19**, 2574
- Zhang, H., Sakurai, T., Pevtsov, A., et al. 2010, *MNRAS*, **402**, L30